Supplement of Atmos. Chem. Phys., 21, 12005–12019, 2021
https://doi.org/10.5194/acp-21-12005-2021-supplement

Supplement of

Highly oxygenated organic molecules produced by the oxidation of benzene and toluene in a wide range of OH exposure and NO$_x$ conditions

Xi Cheng et al.

Correspondence to: Qi Chen (qichenpku@pku.edu.cn) and Yong Jie Li (yongjieli@um.edu.mo)

S1. OH oxidation of benzene and toluene in the absence of NO_x

Scheme S1 shows the major reaction channels for OH oxidation of benzene and toluene, as represented in the Master Chemical Mechanism (MCM) (http://mcm.leeds.ac.uk/MCMv3.3.1/) (Jenkin et al., 2003; Bloss et al., 2005). OH-initiated oxidation of light aromatics such as benzene and toluene occurs mainly via OH addition, with 90% preference (Calvert et al., 2002). The hydroxy-cyclohexadienyl radical so formed can react with O_2 to form a peroxy radical (RO_2), or can react with hydroperoxyl or peroxy radicals (HO_2 or RO_2) to form an alkoxy radical (RO). RO_2 radical formed from the former channel can undergo (Xu and Wang, 2013; Pan and Wang, 2014; Wu et al., 2014; Schwantes et al., 2017): 1) O_2 elimination and go back to the OH-addition adduct; 2) HO_2 elimination to form phenols; 3) cyclization to form bicyclic intermediate (a new alkyl radical); 4) intra-molecular H-shift; and 5) reactions with NO, HO_2, or RO_2 to form an alkoxy radical (RO). A number of studies have suggested that formation of phenols via the HO_2 elimination (pathways 2) and formation of the bicyclic intermediate through cyclization (pathway 3) are major fates of the RO_2 generated (Jenkin et al., 2003; Bloss et al., 2005; Wang et al., 2017), with pathway 2 occurs more rapidly than does pathway 3 (Schwantes et al., 2017). Reactions of the newly formed phenols (e.g., cresol from toluene) can again be initiated by OH radicals, which have rate constants one order of magnitude higher than those of the aromatic precursors. Studies have shown that a major fraction of oxygenated compounds through this pathway has oxygen atoms less than 6 (Calvert et al., 2002; Schwantes et al., 2017; Garmash et al., 2020). The bicyclic intermediate, on the other hand, is a new alkyl radical and can easily undergo O_2 addition to form a new RO_2 radical, analogous to the auto-oxidation of terpenoids or alkanes that forms highly oxygenated organic molecules (HOMs) (Crounse et al., 2013; Ehn et al., 2014; Berndt et al., 2016; Praske et al., 2018; Bianchi et al., 2019). This new RO_2 radical, which has an O-O bridge on a distorted aromatic ring and a (new) R-O-O group on one of the six carbons of the original ring, is termed as the bicyclic peroxy radical (BPR) (Calvert et al., 2002; Birdsall et al., 2010; Wu et al., 2014; Wang et al., 2017) and has been detected in experimental studies (Birdsall et al., 2010; Birdsall and Elrod, 2011; Zaytsev et al., 2019; Garmash et al., 2020).

Schemes S2 and S3 show the proposed mechanism of chain propagation and chain termination reactions from the BPR $C_7H_9O_5$. In Scheme S2, BPR will (1) react with HO_2 or RO_2, forming RO radicals, which eventually decompose into smaller molecules; (2) form new RO_2 radicals through the RO pathway (Sect. S3) or auto-oxidation (H-shift, O_2 addition) pathway. Termination reactions of RO_2 radicals result in HOMs. In Scheme S3, two potential routes for the further oxygen additions to the BPR follow the scheme proposed by Molteni et al. (2018) for mesitylene oxidation. One route represents the traditional auto-oxidation mechanism with internal H abstraction and oxygen addition as described by Wang et al. (2017). The other route involves cyclization forming a second oxygen bridge, which produces a carbon-centered radical followed with the addition of another oxygen molecule (Molteni et al., 2018). Toluene could undergo these two routes for the second step of auto-oxidation occurred after BPRs form because of the methyl group, which is different from benzene.

S2. Methods

Experimental setup

In a typical experiment, the O_3 flow of 0.56 L min^{-1}, the humidified carrier gas flow of 3.3 L min^{-1}, and the N_2O flow of 0.1 L min^{-1} (only for high NO_x) were injected into the oxidation flow reactor (OFR). A small flow of benzene or toluene from gas cylinders was introduced into the OFR to achieve mixing ratios of 110 ppb for benzene and 50 ppb for toluene. The total flow was made up by dry zero air of about 4.3 L min^{-1} to 8.4 L min^{-1}, resulting in an average residence time of 95 s. In the OFR, the voltage for the 254-nm lamp ballast (PAM lamp1) was set to sequentially step from 2 to 10 VDC to generate OH radicals with different concentrations. The voltage for the external ozone lamp ballast was maintained at 3.3 VDC, leading to an O_3

concentration of about 5 ppm at the exit of the OFR (OFR254-5). Figure S2 shows the experimental sequence of a typical OFR254-5 experiment for toluene. The flowrate for VOC injection was regularly set to zero for > 15 min, which we marked as “background” periods. After a full ramping of lamp voltage, the OFR was flushed with humidified zero air at full lamp power (i.e., all lamps at 10 VDC) for at least 4 hours for cleaning.

Photochemical modeling

We used an OFR-based photochemical box model (PAMchem) introduced by Lambe et al. (2017) to estimate the concentrations of reactive species (e.g., OH, HO_2, NO, and NO_2) in the OFR. The actinic flux at 254 nm (I_{254}) is a key parameter for the model. We conducted calibration experiments for SO_2 under low-NO_x (no N_2O addition; OFR254-5) and high-NO_x (1.1% vol N_2O addition; OFR254-5-iN_2O1.1) conditions to determine the I_{254}. SO_2 (5 ppm in N_2) in a gas cylinder was diluted and injected to the OFR. The voltage of PAM lamp 1 was adjusted to achieve various OH exposure. The mixing ratio of SO_2 was measured at the exit of the OFR by a gas analyzer (Thermo, 43i). The integrated OH exposure was calculated from its relative decay. The relative light intensity was monitored by a photodiode in the OFR. We tuned I_{254} in the model to best match the measured quantities. The final model results compared to the measurements are shown in Fig. S3. The model reproduces the measured decay of SO_2. The relationship between I_{254} and measured irradiance is established. For benzene and toluene oxidation under various NO_x conditions, I_{254} ranged from 0.16 to 4.45 × 10^{15} photon cm^{-2} s. Derived steady-state OH exposure ranged from 1.1 × 10^{11} to 2.5 × 10^{12} molecules cm^{-3} s, and HO_2 concentration was in the range of 0.5 to 2.4 ppb. The modeled concentrations of NO and NO_2 are listed in Table S1. Table S1 also summarizes other experimental conditions as well as the measured and derived quantities (Li et al., 2015; Peng et al., 2015; Lambe et al., 2017). According to Lambe et al. (2017), the uncertainty of the estimated OH exposure is about 25%, and those for other modeled quantities are 60%. Thus, the propagated uncertainties for $[NO_x]$:$[HO_2]$ ratios are about 104%.

CIMS data analysis

For the data measured by an Aerodyne time-of-flight chemical ionization mass spectrometer with nitrate as the ionization reagent (NO_3^--TOF-CIMS), three principles were used for data analysis. First, to ensure that signals were truly from the reactions instead of contamination, positive matrix factorization (PMF) analysis was conducted on the unit mass resolution data between mass-to-charge ratio (*m*/*z*, in Th) 150 and 450 by using the Igor PMF evaluation tool (PET, version 3.04A). An example of the time series of identified PMF factors as well as experimental conditions is shown in Fig. S4. Factors that show greater signals during the “background” periods than the reaction periods were considered as non-production factors (background or contamination). The major ions in the spectra of those factors were removed from the final dataset prior to high-resolution fitting. Second, background signals of the oxygenated products were determined by the signals detected during the non-VOC periods. Third, although the formation of NO_3^--adduct ions were preferable in our instrument settings of the NO_3^--TOF-CIMS, the oxygenated products may be detected as adducts with $HNO_3NO_3^-$. This disturbed us when deciding the source of nitrogen atoms of formulas under high-NO_x conditions. With high signals of the reagent ion $HNO_3HNO_3NO_3^-$ in our experiments, we expected that in the fitted ions with two or more nitrogen atoms, the nitrogen atoms were both from the reagent ions if there was a good correlation between the NO_3^--adduct and $HNO_3NO_3^-$-adduct. As shown in Fig. S5a, the ion formula of $C_7H_8N_3O_9^-$ was assigned as $C_7H_7NO_3$-$HNO_3NO_3^-$ instead of $C_7H_8N_2O_6$-NO_3^- because of the good correlation between the NO_3^--adduct and $HNO_3NO_3^-$-adduct of $C_7H_7NO_3$. In Fig. S5b where a poor correlation was observed, the ion formula of $C_7H_{10}N_3O_{12}^-$ was assigned as $C_7H_{10}N_2O_9$-NO_3^-, and the two nitrogen atoms were perhaps originated from the gaseous oxygenated product itself. We also checked the isotope ratios to confirm the formulas, although the isotope signals were sometimes overridden by adjacent peaks. Only NO_3^--adduct ions were presented in this study.

S3. The RO pathway

The formation of the even-oxygen open-shell monomeric products may involve RO pathways. In this pathway, the RO radical is formed from the reaction of RO_2 (with odd oxygen number) with HO_2 (or another RO_2), subtracting one oxygen atom from the RO_2 (R-S1). After that, the newly formed RO (with even oxygen number) isomerizes to a hydroxylated alkyl radical (R-S2) and results in a new RO_2 radical (R'O_2 with even oxygen number) via O_2 addition (R-S3) (Orlando et al., 2003).

$$C_xH_{y+1}O_{2n+1}\ (RO_2) + HO_2 \rightarrow C_xH_{y+1}O_{2n}\ (RO) + OH + O_2 \tag{R-S1}$$

$$C_xH_{y+1}O_{2n}\ (RO) \rightarrow (HO)C_xH_yO_{2n-1}\ (R) \tag{R-S2}$$

$$(HO)C_xH_yO_{2n-1}\ (R) + O_2 \rightarrow (HO)C_xH_yO_{2n+1}\ (\text{i.e.,} C_xH_{y+1}O_{2n+2}, R'O_2) \tag{R-S3}$$

Formation of the closed-shell monomeric product $C_6H_6O_5$ in benzene oxidation might involve the RO pathway by the reaction between $C_6H_7O_5$ (BPR) and HO_2, forming $C_6H_7O_4$ (RO). Then H-shift (isomerization) and O_2 addition follows, and $C_6H_7O_4$ produces a new RO_2 radical with an even oxygen atom number ($C_6H_7O_6$). Xu et al. (2020) reported the formation of $C_6H_7O_6$ by the RO pathway of $C_6H_7O_4$. $C_6H_7O_6$ can be terminated by HO_2 or RO_2 to form the carbonyl of $C_6H_6O_5$.

S4. Calculation of HOM molar yields

We follow the method described by Garmash et al. (2020) to calculate the molar yields of HOM products assuming their concentration has reached steady state at the exit of OFR. Some of the HOM products might not follow this assumption. The calculated molar yields are perhaps the lower. The formation rate of oxygenated products can be expressed as $k_1\gamma$[VOC][OH] (ppt s^{-1}), where k_1 (cm^3 $molecule^{-1}$ s^{-1}) is the VOC-OH reaction rate coefficient; γ (dimensionless) is the fraction of the reaction producing oxygenated products that has been defined as the molar yield; [VOC] is the concentrations of the VOC precursors (ppt); [OH] is the concentrations of OH radicals (molecules cm^{-3}). To calculate the molar yields of HOM products, the loss in the sampling line are corrected. Sampling-loss experiments were conducted in this work following Cheng et al. (2021). In addition, the loss in the OFR are estimated. The loss rate of HOMs, k_{loss} (s^{-1}), includes the loss to the OFR walls (k_{wall}, s^{-1}), the loss to aerosol particles presented in the OFR (i.e., the condensation sink, CS, s^{-1}), and the loss to non-condensable products due to continuous reaction with OH (k_{OHloss}, s^{-1}) (Palm et al., 2016). For steady state, we have

$$\frac{d[\text{HOMs}]}{dt}=0 \tag{S1}$$

Therefore, $k_1\gamma[\text{VOC}][\text{OH}] = k_{\text{loss}}[\text{HOMs}]$. The molar yield can be calculated as

$$\gamma = \frac{k_{\text{loss}}[\text{HOMs}]}{k_1[\text{VOC}][\text{OH}]} \tag{S2}$$

where

$$k_{\text{loss}} = k_{\text{wall}} + \text{CS} + k_{\text{OHloss}} \tag{S3}$$

We use τ_{wall}, τ_{aer} and τ_{OHloss} to represent the characteristic times of HOMs for the loss to the OFR walls, to aerosol particles, and reaction with OH. The first-order loss rate of HOMs to the OFR walls is limited by eddy diffusion. Following the equation described by McMurry and Grosjean (1985), we have

$$k_{\text{wall}} = \frac{1}{\tau_{\text{wall}}} = \frac{A}{V} \cdot \frac{2}{\pi} \cdot \sqrt{k_e D_g} \tag{S4}$$

The OFR surface-area-to-volume ratio (A/V) is 25 m^{-1}. The coefficient of eddy diffusion (k_e) is 0.0042 s^{-1}, estimated by the method described by Brune (2019) and Huang et al. (2018). The molecular diffusion coefficient (D_g) is determined by the diffusion volume (i.e., 122) and the average molecular weight of HOMs (160 g mol^{-1}) for benzene and toluene oxidation, according to Kulmala et al. (1998) and Fuller et al. (1966). Eq. (S4) results in wall loss rate of 0.0028 s^{-1}, corresponding to τ_{wall} of 357 s, which is similar to the wall loss rate of 400-600 s estimated for OFR in previous studies (Lambe et al., 2011; Palm et al., 2016).

As described by Kulmala et al. (2012), the condensation sink can be calculated as follows:

$$\mathrm{CS} = \frac{1}{\tau_{\mathrm{aer}}} = 4\pi D_g \int_0^\infty r\,\beta(r) N(r)\, dr \tag{S5}$$

where r is the radius of particle size bins, $N(r)$ is the particle number size distribution, and $\beta(r)$ is the correction factor for the transition regime. According to the Fuchs-Sutugin approximation, we have

$$\beta = \frac{1+k_n}{1+1.677k_n+1.333k_n^2} \tag{S6}$$

where k_n is the Knudsen number that equals λ_v/r. λ_v is the mean free path of vapor molecules that can be calculated as follows:

$$\lambda_v = 3D_g\sqrt{\frac{\pi m_x}{8kT}} \tag{S7}$$

where m_x denotes the molecular weight of the oxygenated products and k is the Boltzmann constant (Kulmala et al., 1998). Palm et al. (2016) noted that in their high-CS case (OA concentrations > 1.5 µg $\mathrm{m^{-3}}$), the condensation lifetime is shorter than 100 s (i.e., CS > 0.01 $\mathrm{s^{-1}}$). And in a low-CS case (OA concentrations < 0.3 µg $\mathrm{m^{-3}}$), the condensation lifetime is longer than 400 s (i.e., CS < 0.0025 $\mathrm{s^{-1}}$), leading to significantly kinetically limited condensation (Palm et al., 2016; Peng and Jimenez, 2020). The average CS for the experiments herein is 0.07 ± 0.03 $\mathrm{s^{-1}}$, indicating that condensation is an important fate of the HOMs for our experiments.

Finally, similar to the study of Palm et al. (2016), we estimated the continueous reaction loss of HOMs with OH as follows:

$$k_{\mathrm{OHloss}} = \frac{1}{\tau_{\mathrm{OHloss}}} \tag{S8}$$

$$\tau_{\mathrm{OHloss}} = \frac{5}{k_{\mathrm{OH}}[\mathrm{OH}]} \tag{S9}$$

where we assume a rate constant for the reaction of HOMs with OH of 1.0×10^{-11} $\mathrm{cm^3\ molecule^{-1}\ s^{-1}}$ (Ziemann and Atkinson, 2012). Equations (S8) and (S9) result in an average k_{OHloss} of 0.04 ± 0.02 $\mathrm{s^{-1}}$.

S5. Kinetic analysis

Formation of ROOH

Under low-$\mathrm{NO_x}$ conditions and low precursor concentrations (low $\mathrm{RO_2}$), the termination of $\mathrm{RO_2}$ proceeds mainly by $\mathrm{HO_2}$ via reactions of R-S4 to R-S8 (Jenkin et al., 2019).

$$\mathrm{RO_2 + HO_2 \rightarrow ROOH + O_2} \tag{R-S4}$$

$$\mathrm{RO_2 + HO_2 \rightarrow ROH + O_3} \tag{R-S5}$$

$$\mathrm{RO_2 + HO_2 \rightarrow R_{-H}{=}O + H_2O + O_2} \tag{R-S6}$$

$$\mathrm{RO_2 + HO_2 \rightarrow RO + OH + O_2} \tag{R-S7}$$

$$\mathrm{RO_2 + HO_2 \rightarrow R_{-H}{=}O + OH + HO_2} \tag{R-S8}$$

Jenkin et al. (2019) suggested that the overall rate coefficients of $\mathrm{RO_2}$ + $\mathrm{HO_2}$ for benzene and toluene oxidation are 1.92×10^{-11} and 1.98×10^{-11} $\mathrm{cm^3\ molecules^{-1}\ s^{-1}}$ at 298 K, meaning a lifetime of about 1 - 5 s in our experiments. Our OFR experiments have a residence time of about 95 s, which is much longer than the $\mathrm{RO_2}$ termination rate by $\mathrm{HO_2}$. Thus, ROOH at the exit of the OFR can be assumed at steady state, meaning

$$\frac{\mathrm{d[ROOH]}}{\mathrm{dt}} = 0 \tag{S10}$$

Thus,

$$k_{\mathrm{R\text{-}S4}}[\mathrm{RO_2}][\mathrm{HO_2}] = k_{\mathrm{ROOH\_loss}}[\mathrm{ROOH}] \tag{S11}$$

where $k_{\mathrm{R\text{-}S4}}$ ($\mathrm{cm^3\ molecule^{-1}\ s^{-1}}$) is the rate coefficient of Reaction R-S4, and $k_{\mathrm{ROOH\_loss}}$ ($\mathrm{s^{-1}}$) is the loss rate of ROOH. For the benzene-derived $\mathrm{RO_2}$ radical of $\mathrm{C_6H_7O_7}$, we have

$$k_{\mathrm{R\text{-}S4}}[\mathrm{C_6H_7O_7}][\mathrm{HO_2}] = k_{\mathrm{ROOH\_loss}}[\mathrm{C_6H_8O_7}] \tag{S12}$$

$$k_{\mathrm{R\text{-}S4}} = \frac{k_{\mathrm{ROOH\_loss}}[\mathrm{C_6H_8O_7}]}{[\mathrm{HO_2}][\mathrm{C_6H_7O_7}]} \tag{S13}$$

For the toluene-derived RO_2 radical of $C_7H_9O_7$, we have

$$k_{\mathrm{R\text{-}S4}}[\mathrm{C_7H_9O_7}][\mathrm{HO_2}] = k_{\mathrm{ROOH\_loss}}[\mathrm{C_7H_{10}O_7}] \tag{S14}$$

$k_{\mathrm{R\text{-}S4}}$ can therefore be constrained as follows:

$$k_{\mathrm{R\text{-}S4}} = \frac{k_{\mathrm{ROOH\_loss}}[\mathrm{C_7H_{10}O_7}]}{[\mathrm{HO_2}][\mathrm{C_7H_9O_7}]} \tag{S15}$$

The concentrations of RO_2 radicals were detected by the NO_3^--TOF-CIMS. [HO_2] were estimated by the PAMchem model. The $k_{\mathrm{ROOH\_loss}}$ estimation were described in Sect S4. The slopes in Fig. 5a represent the rate coefficients of the hydroperoxide pathway, which are 1.20×10^{-11} and 1.26×10^{-11} $\mathrm{cm^3\ molecules^{-1}\ s^{-1}}$. These rate coefficients indicate the branching ratios for the hydroperoxide formation under low NO_x conditions are 0.62 and 0.64 for benzene- and toluene-derived RO_2 ($C_xH_{y+1}O_7$), respectively, which are consistent with those found in literature (0.52 - 1.00) (Jenkin et al., 2019).

Formation of $RONO_2$ and $ROONO_2$

$$\mathrm{RO_2 + NO \rightarrow RO + NO_2} \tag{R-S9}$$

$$\mathrm{RO_2 + NO(+M) \rightarrow RONO_2(+M)} \tag{R-S10}$$

$$\mathrm{RO_2 + NO_2 \rightleftharpoons ROONO_2} \tag{R-S11}$$

$$\mathrm{RC(O)OO + NO_2 \rightarrow RC(O)OONO_2} \tag{R-S12}$$

The fraction of the reaction proceeding via the terminating channel R-S10 for a specific peroxy radical can be calculated as follows:

$$R_{\mathrm{R\text{-}S10}} = k_{\mathrm{R\text{-}S10}}/(k_{\mathrm{R\text{-}S9}}+k_{\mathrm{R\text{-}S10}}) = f_a f_b(\mathrm{R}^\circ/(1+\mathrm{R}^\circ)) \tag{S16}$$

where R° can be calculated on the basis of temperature and the molecular formula of the peroxy radical. The scaling factors, f_a and f_b, are used to allow for systematic variations in the yields of $RONO_2$ for primary, secondary and tertiary radicals (f_a), and for the presence of oxygenated functional groups (f_b) (Jenkin et al., 2019). For forming hydroxy-dioxa-bicyclo peroxy radical ($C_6H_7O_5$) in benzene oxidation, R° is 0.3722, and f_a and f_b are 1.0 and 0.33, respectively. Thus, $R_{\mathrm{R\text{-}S10}}$ for $C_6H_7O_5$ is 0.0895. For forming the hydroxy-dioxa-bicyclo peroxy radical ($C_7H_9O_5$) in toluene oxidation, R° is 0.3951, and f_a and f_b are 1.0 and 0.33, 0.43 and 0.33, or 0.13 and 0.33, respectively, depending on the position of the substituted groups. Thus, the $R_{\mathrm{R\text{-}S10}}$ for $C_7H_9O_5$ is 0.0935, 0.0402, or 0.0122. Jenkin et al. (2019) suggest a generic rate coefficient of RO_2 + NO at 298 K of 9.04×10^{-12} $\mathrm{cm^3\ molecules^{-1}\ s^{-1}}$. Based on the rate coefficient and the branching ratios above for $C_xH_{y+1}O_5$, the formation rate coefficients of $RONO_2$ ($k_{\mathrm{R\text{-}S10}}$) for the RO_2 radicals of $C_xH_{y+1}O_7$ in our experiments are estimated to be 8.09×10^{-13} and 1.10 - 8.45×10^{-13} $\mathrm{cm^3\ molecules^{-1}\ s^{-1}}$, respectively. Similar to ROOH, $RONO_2$ at the exit of the OFR can be assumed at steady state, meaning

$$\frac{\mathrm{d[RONO_2]}}{\mathrm{dt}} = 0 \tag{S17}$$

$$k_{\mathrm{R\text{-}S10}}[\mathrm{RO_2}][\mathrm{NO}] = k_{\mathrm{RONO_2\_loss}}[\mathrm{RONO_2}] \tag{S18}$$

where $k_{\mathrm{RONO_2\_loss}}$ ($\mathrm{s^{-1}}$) is the loss rate of the $RONO_2$. We then have

$$\frac{[\mathrm{RONO_2}]}{[\mathrm{ROOH}]} = \frac{k_{\mathrm{R\text{-}S10}}}{k_{\mathrm{R\text{-}S4}}} \times \frac{k_{\mathrm{ROOH\_loss}}}{k_{\mathrm{RONO_2\_loss}}} \times \frac{[\mathrm{NO}]}{[\mathrm{HO_2}]} \tag{S19}$$

$k_{\mathrm{ROOH\_loss}}$ and $k_{\mathrm{RONO_2\_loss}}$ are expectedly similar because of similar molecular weights and oxygen contents for ROOH and $RONO_2$ in the same experiment. Therefore, we have:

$$\frac{[\mathrm{RONO_2}]}{[\mathrm{ROOH}]} = \frac{k_{\mathrm{R\text{-}S10}}}{k_{\mathrm{R\text{-}S4}}} \times \frac{[\mathrm{NO}]}{[\mathrm{HO_2}]} \tag{S20}$$

For the benzene-derived RO_2 radical $C_6H_7O_7$, we have

$$\frac{[\mathrm{C_6H_7NO_8}]}{[\mathrm{C_6H_8O_7}]} = \frac{k_{\mathrm{R\text{-}S10}}}{k_{\mathrm{R\text{-}S4}}} \times \frac{[\mathrm{NO}]}{[\mathrm{HO_2}]} \tag{S21}$$

For the toluene-derived RO_2 radical $C_7H_9O_7$, we have

$$\frac{[C_7H_9NO_8]}{[C_7H_{10}O_7]} = \frac{k_{\text{R-S10}}}{k_{\text{R-S4}}} \times \frac{[NO]}{[HO_2]} \tag{S22}$$

Here, the concentrations of HOMs were detected by NO_3^--TOF-CIMS. [NO] and [HO_2] were estimated by the PAMchem model. Similar to the analysis of the ROOH formation, the slopes in Fig. 5b suggest that the formation rate coefficients of $RONO_2$ are 2.87×10^{-11} and 6.12×10^{-11} cm^3 $molecules^{-1}$ s^{-1} for benzene and toluene oxidation under our OFR254-5-iN_2O1.1 conditions, respectively. These coefficients are more than one order of magnitude greater than the values estimated above from the literature (i.e., 8.09×10^{-13} and 1.10 - 8.45×10^{-13} cm^3 $molecules^{-1}$ s^{-1} for benzene and toluene oxidation, respectively) (Jenkin et al., 2019).

References

Berndt, T., Richters, S., Jokinen, T., Hyttinen, N., Kurten, T., Otkjaer, R. V., Kjaergaard, H. G., Stratmann, F., Herrmann, H., Sipila, M., Kulmala, M., and Ehn, M.: Hydroxyl radical-induced formation of highly oxidized organic compounds, Nat. Commun., 7, 13677, https://doi.org/10.1038/ncomms13677, 2016.

Bianchi, F., Kurten, T., Riva, M., Mohr, C., Rissanen, M. P., Roldin, P., Berndt, T., Crounse, J. D., Wennberg, P. O., Mentel, T. F., Wildt, J., Junninen, H., Jokinen, T., Kulmala, M., Worsnop, D. R., Thornton, J. A., Donahue, N., Kjaergaard, H. G., and Ehn, M.: Highly oxygenated organic molecules (HOM) from gas-phase autoxidation involving peroxy radicals: a key contributor to atmospheric aerosol, Chem. Rev., 119, 3472-3509, https://doi.org/10.1021/acs.chemrev.8b00395, 2019.

Birdsall, A. W., Andreoni, J. F., and Elrod, M. J.: Investigation of the role of bicyclic peroxy radicals in the oxidation mechanism of toluene, J. Phys. Chem. A, 114, 10655-10663, https://doi.org/10.1021/jp105467e, 2010.

Birdsall, A. W., and Elrod, M. J.: Comprehensive NO-dependent study of the products of the oxidation of atmospherically relevant aromatic compounds, J. Phys. Chem. A, 115, 5397-5407, https://doi.org/10.1021/jp2010327, 2011.

Bloss, C., Wagner, V., Jenkin, M. E., Volkamer, R., Bloss, W. J., Lee, J. D., Heard, D. E., Wirtz, K., Martin-Reviejo, M., Rea, G., Wenger, J. C., and Pilling, M. J.: Development of a detailed chemical mechanism (MCMv3.1) for the atmospheric oxidation of aromatic hydrocarbons, Atmos. Chem. Phys., 5, 641-664, https://doi.org/10.5194/acp-5-641-2005, 2005.

Brune, W. H.: The chamber wall index for gas-wall interactions in atmospheric environmental enclosures, Environ. Sci. Technol., 53, 3645-3652, https://doi.org/10.1021/acs.est.8b06260, 2019.

Calvert, J. G., Atkinson, R., Becker, K. H., Kamens, R. M., Seinfeld, J. H., Wallington, T. J., and Yarwood, G. Y.: The mechanisms of atmospheric oxidation of aromatic hydrocarbons, Oxford University Press, New York, 2002.

Cheng, X., Chen, Q., Li, Y., Huang, G., Liu, Y., Lu, S., Zheng, Y., Qiu, W., Lu, K., Qiu, X., Bianchi, F., Yan, C., Yuan, B., Shao, M., Wang, Z., Canagaratna, M. R., Zhu, T., Wu, Y., and Zeng, L.: Secondary Production of Gaseous Nitrated Phenols in Polluted Urban Environments, Environ. Sci. Technol., 55, 4410-4419, https://doi.org/10.1021/acs.est.0c07988, 2021.

Crounse, J. D., Nielsen, L. B., Jørgensen, S., Kjaergaard, H. G., and Wennberg, P. O.: Autoxidation of organic compounds in the atmosphere, J. Phys. Chem. Lett., 4, 3513-3520, https://doi.org/10.1021/jz4019207, 2013.

Ehn, M., Thornton, J. A., Kleist, E., Sipila, M., Junninen, H., Pullinen, I., Springer, M., Rubach, F., Tillmann, R., Lee, B., Lopez-Hilfiker, F., Andres, S., Acir, I. H., Rissanen, M., Jokinen, T., Schobesberger, S., Kangasluoma, J., Kontkanen, J., Nieminen, T., Kurten, T., Nielsen, L. B., Jorgensen, S., Kjaergaard, H. G., Canagaratna, M., Dal Maso, M., Berndt, T., Petaja, T., Wahner, A., Kerminen, V. M., Kulmala, M., Worsnop, D. R., Wildt, J., and Mentel, T. F.: A large source of low-volatility secondary organic aerosol, Nature, 506, 476-479, https://doi.org/10.1038/nature13032, 2014.

Fuller, E. N., Schettler, P. D., and Giddings, J. C.: A new method for prediction of binary gas-phase diffusion coefficients, Ind. Eng. Chem., 58, 18-27, https://doi.org/10.1021/ie50677a007, 1966.

Garmash, O., Rissanen, M. P., Pullinen, I., Schmitt, S., Kausiala, O., Tillmann, R., Zhao, D., Percival, C., Bannan, T. J., Priestley, M., Hallquist, Å. M., Kleist, E., Kiendler-Scharr, A., Hallquist, M., Berndt, T., McFiggans, G., Wildt, J., Mentel, T. F., and Ehn, M.: Multi-generation OH oxidation as a source for highly oxygenated organic molecules from aromatics, Atmos. Chem. Phys., 20, 515-537, https://doi.org/10.5194/acp-20-515-2020, 2020.

Huang, M. Q., Lin, Y. H., Huang, X. Y., Liu, X. Q., Hu, C. J., Gu, X. J., Zhao, W. X., Fang, L., and Zhang, W. J.: Chemical analysis of aged benzene secondary organic aerosol using aerosol laser time-of-flight mass spectrometer, J. Atmos. Chem., 71, 213-224, https://doi.org/10.1007/s10874-014-9291-z, 2014.

Huang, Y. L., Zhao, R., Charan, S. M., Kenseth, C. M., Zhang, X., and Seinfeld, J. H.: Unified theory of vapor-wall mass transport in teflon-walled environmental chambers, Environ. Sci. Technol., 52, 2134-2142, https://doi.org/10.1021/acs.est.7b05575, 2018.

Jenkin, M. E., Saunders, S. M., Wagner, V., and Pilling, M. J.: Protocol for the development of the Master Chemical Mechanism, MCM v3 (Part B): tropospheric degradation of aromatic volatile organic compounds, Atmos. Chem. Phys., 3, 181-193, https://doi.org/10.5194/acp-3-181-2003, 2003.

Jenkin, M. E., Valorso, R., Aumont, B., and Rickard, A. R.: Estimation of rate coefficients and branching ratios for reactions of organic peroxy radicals for use in automated mechanism construction, Atmos. Chem. Phys., 19, 7691-7717, https://doi.org/10.5194/acp-19-7691-2019, 2019.

Kulmala, M., Toivonen, A., Mäkelä, J. M., and Laaksonen, A.: Analysis of the growth of nucleation mode particles observed in boreal forest, Tellus B, 50, 449-462, https://doi.org/10.3402/tellusb.v50i5.16229, 1998.

Kulmala, M., Petäjä, T., Nieminen, T., Sipilä, M., Manninen, H. E., Lehtipalo, K., Dal Maso, M., Aalto, P. P., Junninen, H., Paasonen, P., Riipinen, I., Lehtinen, K. E. J., Laaksonen, A., and Kerminen, V.-M.: Measurement of the nucleation of atmospheric aerosol particles, Nat. Protoc., 7, 1651-1667, https://doi.org/10.1038/nprot.2012.091, 2012.

Lambe, A., Massoli, P., Zhang, X., Canagaratna, M., Nowak, J., Daube, C., Yan, C., Nie, W., Onasch, T., Jayne, J., Kolb, C., Davidovits, P., Worsnop, D., and Brune, W.: Controlled nitric oxide production via O(1-D) + N2O reactions for use in oxidation flow reactor studies, Atmos. Meas. Tech., 10, 2283-2298, https://doi.org/10.5194/amt-10-2283-2017, 2017.

Lambe, A. T., Ahern, A. T., Williams, L. R., Slowik, J. G., Wong, J. P. S., Abbatt, J. P. D., Brune, W. H., Ng, N. L., Wright, J. P., Croasdale, D. R., Worsnop, D. R., Davidovits, P., and Onasch, T. B.: Characterization of aerosol photooxidation flow reactors: heterogeneous oxidation, secondary organic aerosol formation and cloud condensation nuclei activity measurements, Atmos. Meas. Tech., 4, 445-461, https://doi.org/10.5194/amt-4-445-2011, 2011.

Li, R., Palm, B. B., Ortega, A. M., Hlywiak, J., Hu, W. W., Peng, Z., Day, D. A., Knote, C., Brune, W. H., de Gouw, J. A., and Jimenez, J. L.: Modeling the radical chemistry in an oxidation flow reactor: radical formation and recycling, sensitivities, and the OH exposure estimation equation, J. Phys. Chem. A, 119, 4418-4432, https://doi.org/10.1021/jp509534k, 2015.

McMurry, P. H., and Grosjean, D.: Gas and aerosol wall losses in Teflon film smog chambers, Environ. Sci. Technol., 19, 1176-1182, https://doi.org/10.1021/es00142a006, 1985.

Mehra, A., Wang, Y., Krechmer, J. E., Lambe, A., Majluf, F., Morris, M. A., Priestley, M., Bannan, T. J., Bryant, D. J., Pereira, K. L., Hamilton, J. F., Rickard, A. R., Newland, M. J., Stark, H., Croteau, P., Jayne, J. T., Worsnop, D. R., Canagaratna, M. R., Wang, L., and Coe, H.: Evaluation of the chemical composition of gas- and particle-phase products of aromatic oxidation, Atmos. Chem. Phys., 20, 9783-9803, https://doi.org/10.5194/acp-20-9783-2020, 2020.

Molteni, U., Bianchi, F., Klein, F., El Haddad, I., Frege, C., Rossi, M. J., Dommen, J., and Baltensperger, U.: Formation of highly oxygenated organic molecules from aromatic compounds, Atmos. Chem. Phys., 18, 1909-1921, https://doi.org/10.5194/acp-18-1909-2018, 2018.

Orlando, J. J., Tyndall, G. S., and Wallington, T. J.: The atmospheric chemistry of alkoxy radicals, Chem. Rev., 103, 4657-4690, https://doi.org/10.1021/cr020527p, 2003.

Palm, B. B., Campuzano-Jost, P., Ortega, A. M., Day, D. A., Kaser, L., Jud, W., Karl, T., Hansel, A., Hunter, J. F., Cross, E. S., Kroll, J. H., Peng, Z., Brune, W. H., and Jimenez, J. L.: In situ secondary organic aerosol formation from ambient pine forest air using an oxidation flow reactor, Atmos. Chem. Phys., 16, 2943-2970, https://doi.org/10.5194/acp-16-2943-2016, 2016.

Pan, S., and Wang, L.: Atmospheric oxidation mechanism of m-xylene initiated by OH radical, J. Phys. Chem. A, 118, 10778-10787, https://doi.org/10.1021/jp506815v, 2014.

Peng, Z., Day, D. A., Stark, H., Li, R., Lee-Taylor, J., Palm, B. B., Brune, W. H., and Jimenez, J. L.: HOx radical chemistry in oxidation flow reactors with low-pressure mercury lamps systematically examined by modeling, Atmos. Meas. Tech., 8, 4863-4890, https://doi.org/10.5194/amt-8-4863-2015, 2015.

Peng, Z., and Jimenez, J. L.: Radical chemistry in oxidation flow reactors for atmospheric chemistry research, Chem. Soc. Rev., 49, 2570-2616, https://doi.org/10.1039/c9cs00766k, 2020.

Praske, E., Otkjær, R. V., Crounse, J. D., Hethcox, J. C., Stoltz, B. M., Kjaergaard, H. G., and Wennberg, P. O.: Atmospheric autoxidation is increasingly important in urban and suburban North America, Proc. Natl. Acad. Sci. U. S. A., 115, 64-69, https://doi.org/10.1073/pnas.1715540115, 2018.

Schwantes, R. H., Schilling, K. A., McVay, R. C., Lignell, H., Coggon, M. M., Zhang, X., Wennberg, P. O., and Seinfeld, J. H.: Formation of highly oxygenated low-volatility products from cresol oxidation, Atmos. Chem. Phys., 17, 3453-3474, https://doi.org/10.5194/acp-17-3453-2017, 2017.

Tsiligiannis, E., Hammes, J., Salvador, C. M., Mentel, T. F., and Hallquist, M.: Effect of NOx on 1,3,5-trimethylbenzene (TMB) oxidation product distribution and particle formation, Atmos. Chem. Phys., 19, 15073-15086, https://doi.org/10.5194/acp-19-15073-2019, 2019.

Wang, S., Wu, R., Berndt, T., Ehn, M., and Wang, L.: Formation of highly oxidized radicals and multifunctional products from the atmospheric oxidation of alkylbenzenes, Environ. Sci. Technol., 51, 8442-8449, https://doi.org/10.1021/acs.est.7b02374, 2017.

Wu, R., Pan, S., Li, Y., and Wang, L.: Atmospheric oxidation mechanism of toluene, J. Phys. Chem. A, 118, 4533-4547, https://doi.org/10.1021/jp500077f, 2014.

Xu, C., and Wang, L.: Atmospheric oxidation mechanism of phenol initiated by OH radical, J. Phys. Chem. A, 117, 2358-2364, https://doi.org/10.1021/jp308856b, 2013.

Xu, L., Møller, K. H., Crounse, J. D., Kjaergaard, H. G., and Wennberg, P. O.: New insights into the radical chemistry and product distribution in the OH-initiated oxidation of benzene, Environ. Sci. Technol., 54, 13467-13477, https://doi.org/10.1021/acs.est.0c04780, 2020.

Zaytsev, A., Koss, A. R., Breitenlechner, M., Krechmer, J. E., Nihill, K. J., Lim, C. Y., Rowe, J. C., Cox, J. L., Moss, J., Roscioli, J. R., Canagaratna, M. R., Worsnop, D. R., Kroll, J. H., and Keutsch, F. N.: Mechanistic study of the formation of ring-retaining and ring-opening products from the oxidation of aromatic compounds under urban atmospheric conditions, Atmos. Chem. Phys., 19, 15117-15129, https://doi.org/10.5194/acp-19-15117-2019, 2019.

Ziemann, P. J., and Atkinson, R.: Kinetics, products, and mechanisms of secondary organic aerosol formation, Chem. Soc. Rev., 41, 6582-6605, https://doi.org/10.1039/C2CS35122F, 2012.

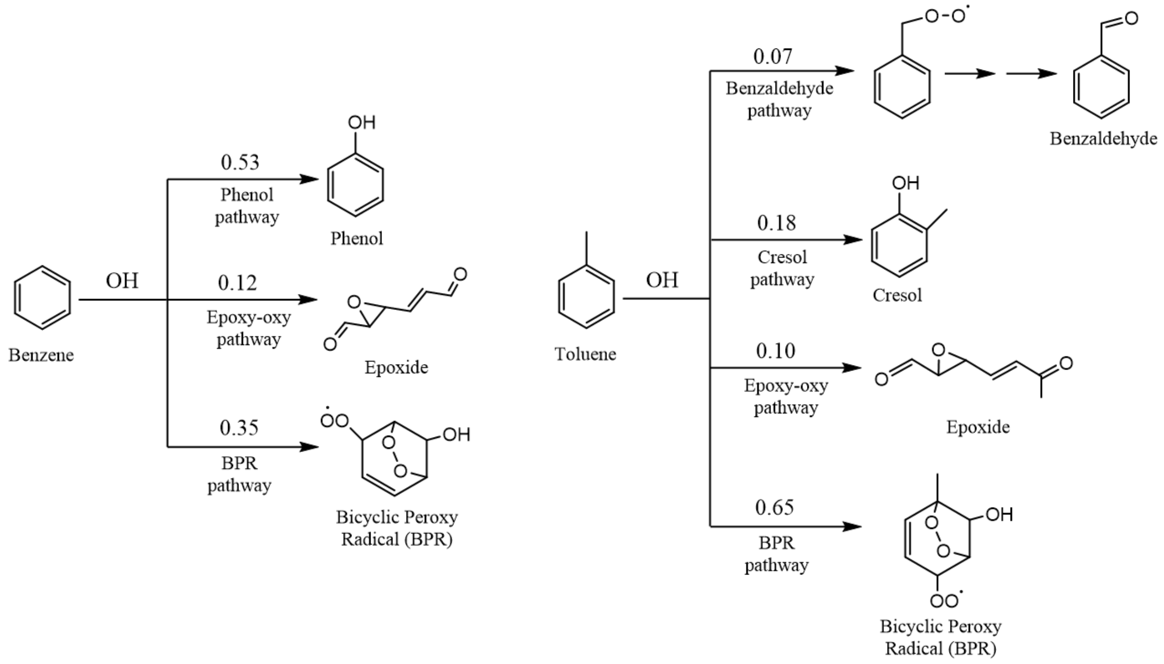

Scheme S1. Major gas-phase oxidation pathways for benzene and toluene in the MCM.

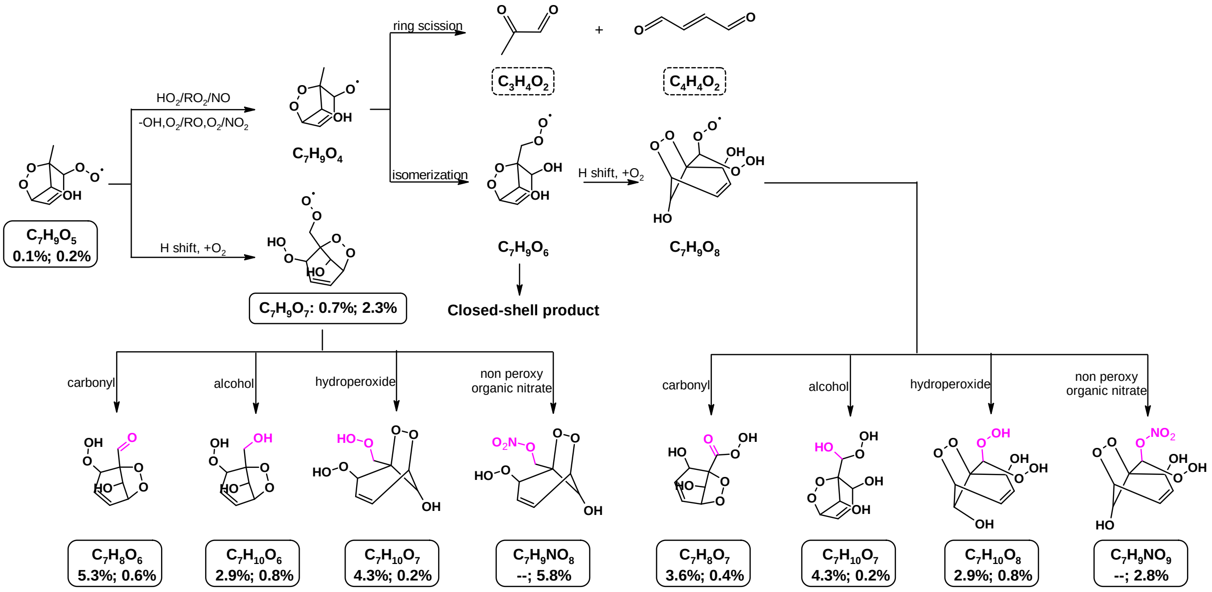

Scheme S2. A proposed mechanism involving the BPR $C_7H_9O_5$. The products shown in the box with dash and solid lines are measured by the PTR-QiTOF and the NO_3^--TOF-CIMS, respectively. Numbers in the box represent the percentages of this molecule in total fitted ion signals for the OFR254-5 and OFR254-5-iN_2O4.4 experiments (Table S3). The functional groups shown in magenta represent the termination pathways.

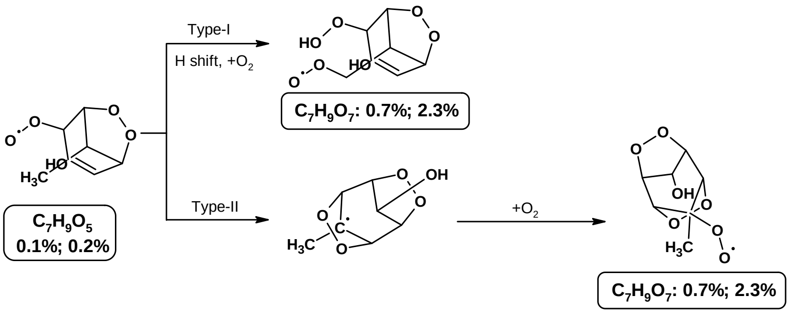

Scheme S3. The proposed mechanism of further auto-oxidation from the BPR $C_7H_9O_5$. Type I and Type II pathways are proposed by Wang et al. (2017) and Molteni et al. (2018).

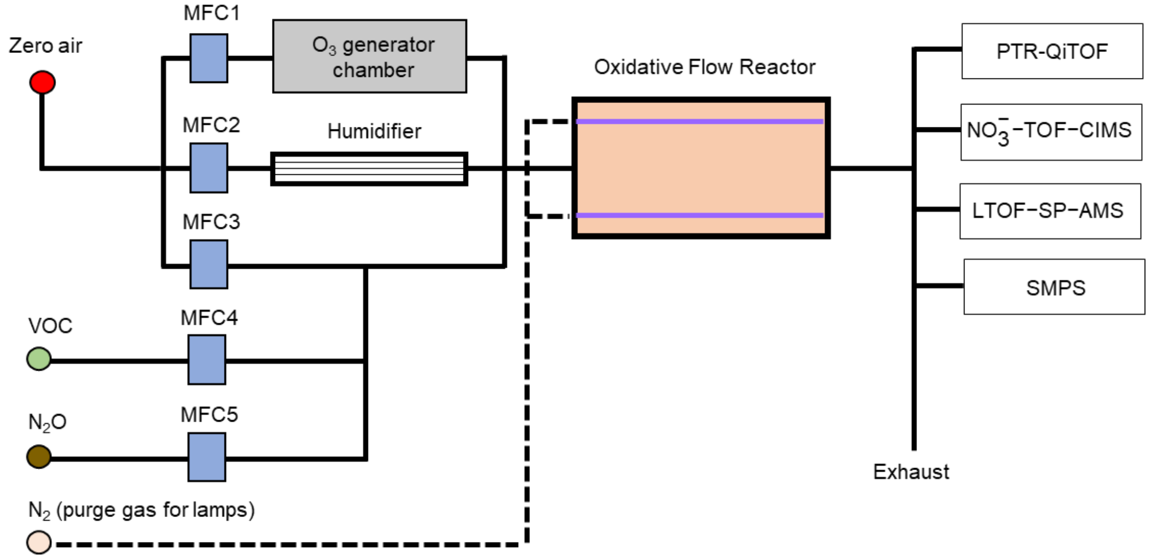

330 **Figure S1.** Schematic of the experimental setup of the benzene and toluene oxidation.

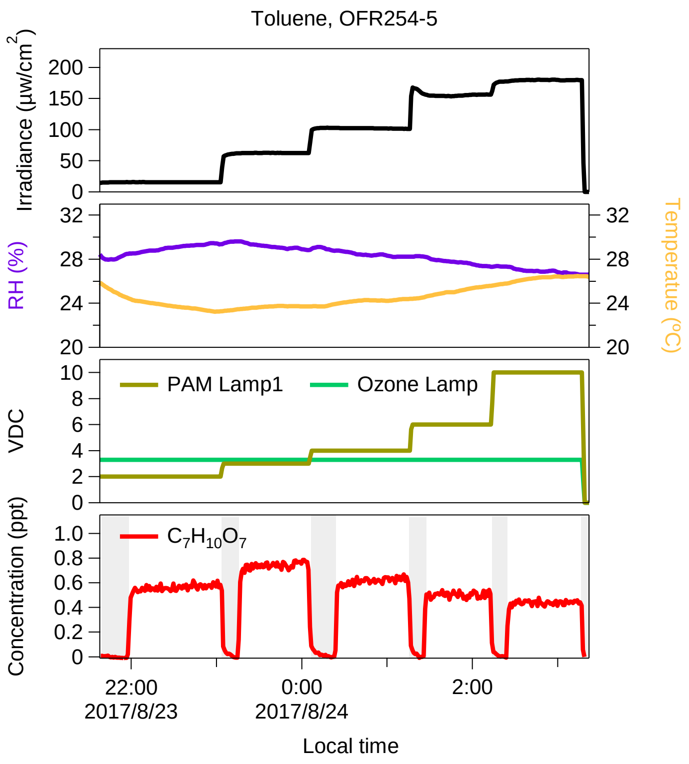

Figure S2. Time series of experimental conditions and an example HOM product for a typical OFR254-5 experiment of toluene oxidation under low-NO_x conditions. The grey shaded area represents "background" periods without VOC injection.

335

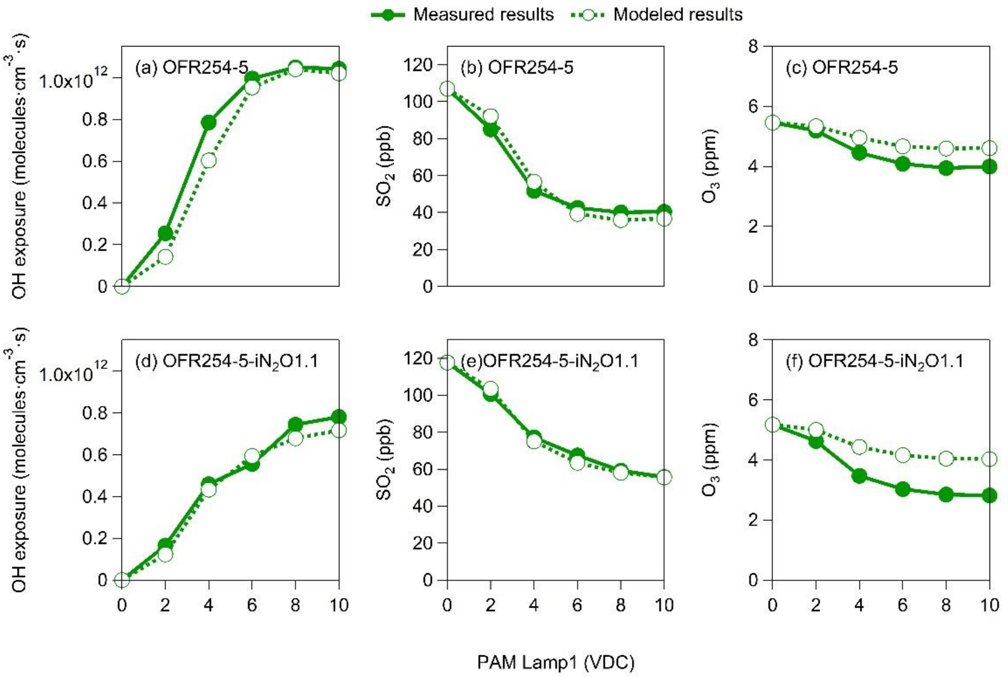

Figure S3. Measured and modeled results of OH exposure, SO_2 and O_3 concentrations for OFR254-5 and OFR254-5-iN_2O1.1 calibration experiments.

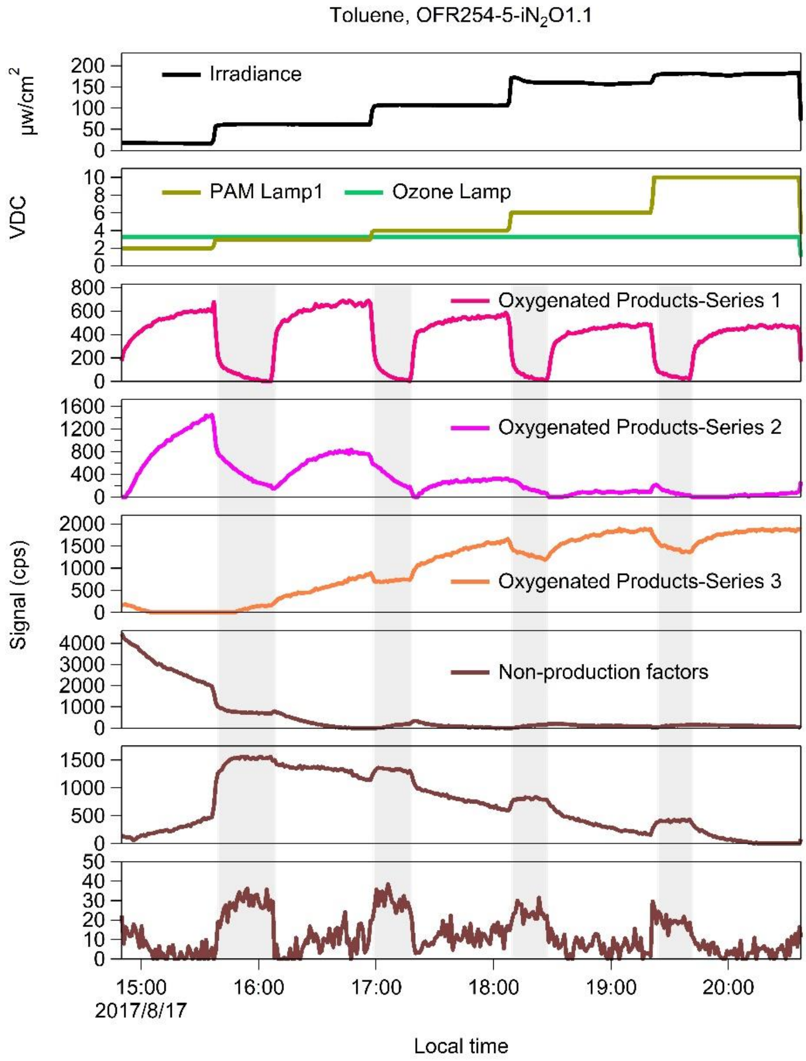

Figure S4. An example of PMF analysis for toluene oxidation under high-NO_x conditions (OFR254-5-iN_2O1.1). The grey shaded areas represent "background" periods without VOC injection.

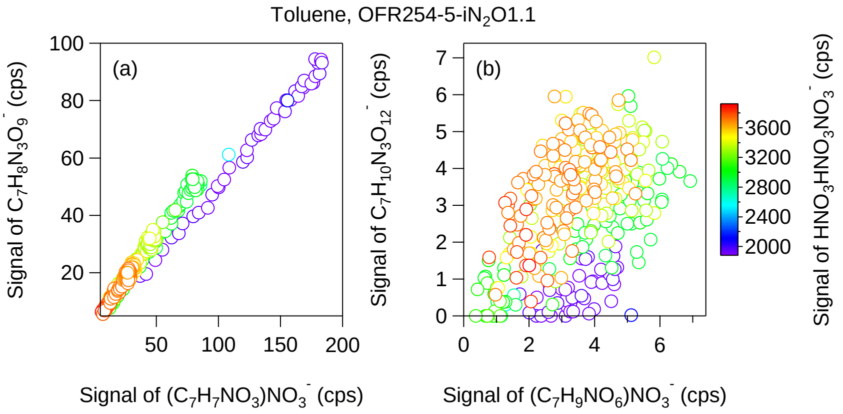

Figure S5. (a) A good correlation between the signals of NO_3^--adduct ($C_7H_7NO_3$-NO_3^-) and $HNO_3NO_3^-$-adduct ($C_7H_7NO_3$-$HNO_3NO_3^-$) ions and (b) a poor correlation between the signals of NO_3^--adduct ($C_7H_9NO_6$-NO_3^-) and NO_3^--adduct ($C_7H_{10}N_2O_9$-NO_3^-) ions for an example toluene oxidation experiment under high-NO_x (OFR254-5-iN$_2$O1.1) conditions.

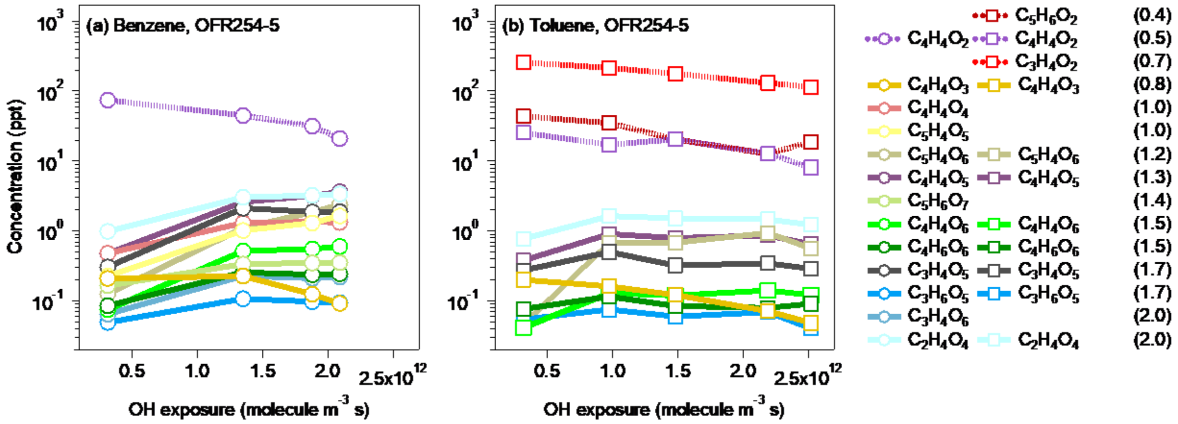

Figure S6. Concentrations of individual fragmented products as OH exposure increases under low-NO$_x$ (OFR254-5) conditions for benzene and toluene oxidation. The products shown in dash lines with symbols were quantified by the PTR-QiTOF, and the products shown in solid lines with symbols were quantified by the NO_3^--TOF-CIMS. The numbers in parentheses refer to the O:C ratios of the molecules.

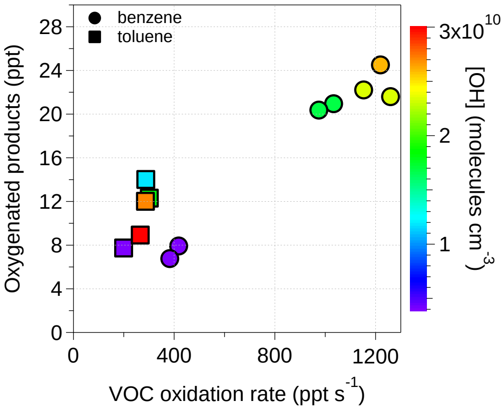

355 **Figure S7.** Scatter plot of the concentrations of total HOMs detected by the NO_3^--TOF-CIMS and the VOC oxidation rates of benzene and toluene oxidation under low-NO_x (OFR254-5) conditions.

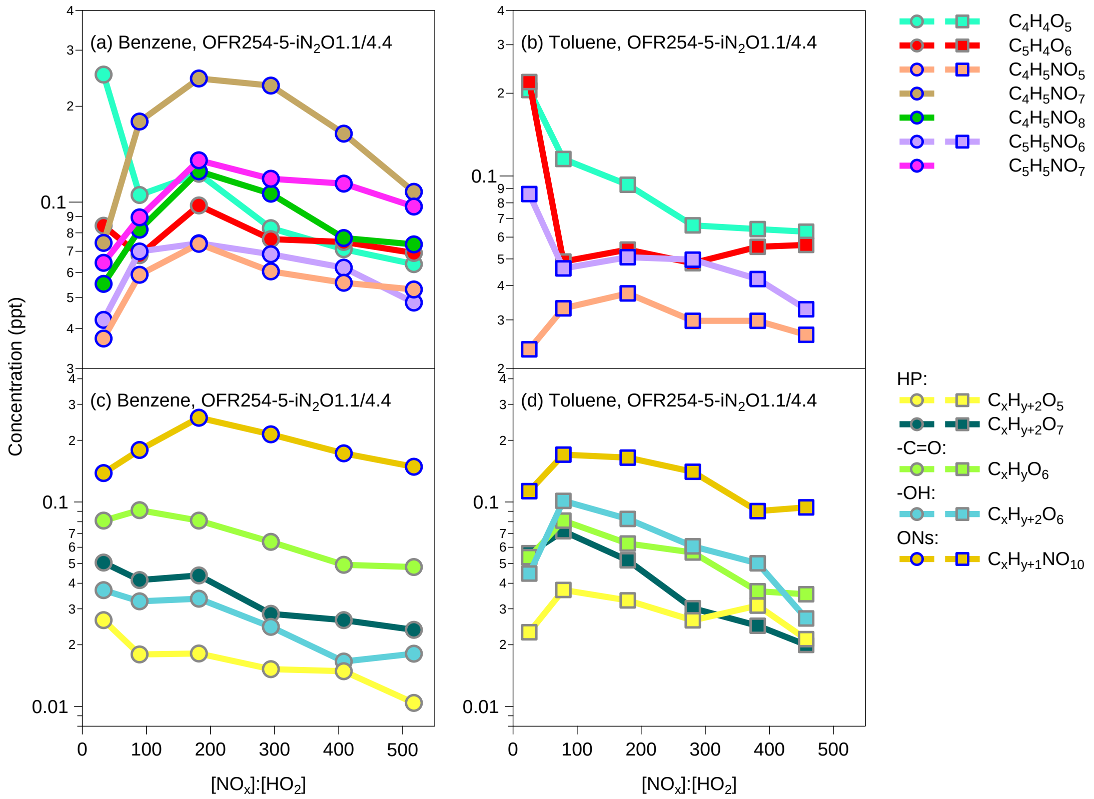

Figure S8. Concentrations of ring-scission and ring-retaining products measured by the NO_3^--TOF-CIMS for increasing [NO$_x$]:[HO$_2$] ratio for benzene and toluene oxidation under high-NO$_x$ conditions. HP: hydroperoxide; -C=O: carbonyl; -OH: alcohol; ONs: organic nitrates.

Table S1. Experimental conditions, measured and derived quantities in the OFR. The terms B and T represent benzene and toluene, respectively. Oxygenated products represent the sum of fragmented, closed-shell monomeric, open-shell monomeric, dimeric, and nitrogen-containing (if any) products measured by the NO_3^--TOF-CIMS.

		Experimental conditions			Measured quantities		Derived quantities			
Exp. No	VOC-Lamp voltage (V)	N_2O_{in} (%, v/v)	RH (%)	Temperature (°C)	ΔVOC (ppb)	Oxygenated products (ppt)	OH_{exp} (molec cm^{-3} s)	HO_2 (ppb)	NO (ppb)	NO_2 (ppb)
1*	B-2	0	23.6	25.0	32.3	6.8	3.1×10^{11}	1.5	/	/
2*	B-4	0	24.3	24.4	64.7	20.4	1.4×10^{12}	2.3	/	/
3*	B-6	0	24.0	25.0	72.2	22.2	1.9×10^{12}	2.4	/	/
4*	B-10	0	23.4	25.6	74.3	24.5	2.1×10^{12}	2.4	/	/
5*	B-2	1.1	25.3	22.9	20.2	18.6	1.1×10^{11}	0.8	0.2	17.4
6*	B-4	1.1	24.7	24.1	36.7	13.0	4.1×10^{11}	1.3	0.9	46.0
7*	B-6	1.1	23.6	25.8	41.9	9.9	5.8×10^{11}	1.4	1.4	49.9
8*	B-10	1.1	23.0	26.8	37.0	7.8	6.5×10^{11}	1.4	1.5	50.3
9$^\#$	B-2	4.4	49.7	23.8	27.4	17.9	1.4×10^{11}	0.7	0.6	60.5
10$^\#$	B-3	4.4	51.0	23.7	31.3	20.7	2.8×10^{11}	0.7	1.8	126.1
11$^\#$	B-4	4.4	48.5	24.7	33.8	15.0	3.7×10^{11}	0.6	3.2	176.1
12$^\#$	B-6	4.4	47.6	25.3	35.6	11.7	4.4×10^{11}	0.5	4.4	208.1
13$^\#$	B-10	4.4	46.0	25.7	36.3	9.9	4.6×10^{11}	0.5	5.1	231.4
14	T-2	0	29.4	23.4	18.5	7.7	3.2×10^{11}	1.5	/	/
15	T-3	0	29.0	23.7	25.8	14.0	9.8×10^{11}	2.2	/	/
16	T-4	0	28.3	24.3	27.8	12.3	1.5×10^{12}	2.3	/	/
17	T-6	0	27.5	25.4	29.4	12.0	2.2×10^{12}	2.3	/	/
18	T-10	0	26.8	26.4	30.0	8.9	2.5×10^{12}	2.2	/	/
19	T-2	1.1	27.2	25.1	22.1	8.0	1.4×10^{11}	0.9	0.2	15.8
20	T-3	1.1	28.3	24.2	32.2	6.1	3.4×10^{11}	1.3	0.5	31.5
21	T-4	1.1	27.8	24.9	35.6	4.6	5.0×10^{11}	1.4	0.9	37.5
22	T-6	1.1	26.8	25.7	36.7	3.6	6.8×10^{11}	1.5	1.3	41.6
23	T-10	1.1	26.2	26.1	36.5	3.3	7.4×10^{11}	1.5	1.5	43.1
24$^\#$	T-2	4.4	55.1	22.3	28.2	9.7	1.4×10^{11}	0.7	0.5	53.0
25$^\#$	T-3	4.4	54.5	22.7	30.3	10.3	2.9×10^{11}	0.7	1.9	123.2
26$^\#$	T-4	4.4	52.9	23.2	31.4	9.3	3.7×10^{11}	0.6	3.0	166.6
27$^\#$	T-6	4.4	51.7	23.8	32.2	8.0	4.3×10^{11}	0.5	4.1	196.3
28$^\#$	T-10	4.4	50.5	24.5	32.8	6.6	4.8×10^{11}	0.5	4.9	213.2

* Experiments that have repeated ones.

$^\#$ Experiments that do not have PTR-QiTOF measurements.

Table S2. The peak list and relative signal contributions (%) of major gaseous products produced by the benzene oxidation experiments shown in Fig. 1a-b.

Category	Formula	*m*/*z* (Th)	Percentage in total fitted signal		Listed by other studies of aromatic oxidation
			Exp. #2* (low NO_x)	Exp. #11$^\#$ (high NO_x)	
Fragmented product	$C_2H_4O_4$	154.00	14.7%	1.3%	
	$C_4H_4O_4$	178.00	6.2%	1.6%	Mehra et al. (2020)
	$C_3H_4O_5$	181.99	9.9%	0.2%	Mehra et al. (2020)
	$C_4H_2O_5$	191.98	2.1%	3.5%	
	$C_4H_4O_5$	193.99	12.9%	0.6%	Schwantes et al. (2017) Mehra et al. (2020)
	$C_4H_6O_5$	196.01	2.3%	0.1%	Mehra et al. (2020)
	$C_5H_4O_5$	205.99	5.0%	0.4%	Mehra et al. (2020)
	$C_5H_6O_5$	208.01	1.6%	0.1%	Schwantes et al. (2017) Mehra et al. (2020)
	$C_4H_4O_6$	209.99	2.5%	0.5%	Mehra et al. (2020)
	$C_4H_6O_6$	212.01	1.2%	0.1%	Mehra et al. (2020)
	$C_5H_4O_6$	221.99	5.7%	0.5%	Mehra et al. (2020)
	$C_5H_6O_7$	240.00	1.6%	0.3%	Molteni et al. (2018) Garmash et al. (2020)
Closed-shell monomeric product	$C_6H_6O_4$	204.02	0.1%	/	Mehra et al. (2020)
	$C_6H_4O_5$	217.99	0.3%	0.1%	Mehra et al. (2020)
	$C_6H_6O_5$	220.01	3.2%	0.4%	Molteni et al. (2018) Mehra et al. (2020)
	$C_6H_8O_5$	222.03	0.4%	0.01%	Molteni et al. (2018) Garmash et al. (2020) Mehra et al. (2020)
	$C_6H_4O_6$	233.99	0.7%	0.2%	Mehra et al. (2020)
	$C_6H_6O_6$	236.01	3.0%	0.4%	Molteni et al. (2018) Mehra et al. (2020)
	$C_6H_8O_6$	238.02	1.8%	0.2%	Molteni et al. (2018) Mehra et al. (2020)
	$C_6H_{10}O_6$	240.04	0.1%	0.04%	
	$C_6H_4O_7$	249.98	0.8%	0.2%	
	$C_6H_6O_7$	252.00	2.6%	0.3%	Molteni et al. (2018) Mehra et al. (2020)
	$C_6H_8O_7$	254.02	2.4%	0.2%	Molteni et al. (2018) Garmash et al. (2020)
	$C_6H_{10}O_7$	256.03	0.5%	0.03%	
	$C_6H_4O_8$	265.98	0.3%	0.04%	
	$C_6H_6O_8$	268.00	1.3%	0.4%	
	$C_6H_8O_8$	270.01	1.9%	0.2%	Molteni et al. (2018) Garmash et al. (2020)
	$C_6H_{10}O_8$	272.03	0.8%	0.1%	Molteni et al. (2018)
	$C_6H_6O_9$	283.99	0.6%	0.04%	
	$C_6H_8O_9$	286.01	1.1%	0.3%	Molteni et al. (2018) Garmash et al. (2020)
	$C_6H_{10}O_9$	288.02	0.4%	/	
	$C_6H_6O_{10}$	299.98	0.2%	0.1%	
	$C_6H_8O_{10}$	302.00	0.4%	0.1%	Molteni et al. (2018)
	$C_6H_{10}O_{10}$	304.02	0.2%	0.1%	
Open-shell monomeric product	$C_6H_7O_5$	221.02	0.1%	0.01%	Garmash et al. (2020)
	$C_6H_5O_6$	235.00	0.4%	0.1%	
	$C_6H_5O_7$	250.99	0.8%	/	
	$C_6H_7O_7$	253.01	0.4%	0.2%	Garmash et al. (2020)
	$C_6H_7O_9$	285.00	0.7%	0.5%	Molteni et al. (2018) Garmash et al. (2020)
	$C_6H_7O_{10}$	300.99	0.5%	0.2%	
Dimeric product	$C_{12}H_{14}O_8$	348.06	0.06%	/	Molteni et al. (2018) Garmash et al. (2020)
	$C_{12}H_{12}O_{10}$	378.03	0.14%	0.04%	
	$C_{12}H_{14}O_{10}$	380.05	0.13%	0.01%	Molteni et al. (2018)

					Garmash et al. (2020)
	$C_{12}H_{12}O_{11}$	394.03	0.10%	0.01%	
	$C_{12}H_{14}O_{11}$	396.04	0.16%	/	Molteni et al. (2018)
	$C_{12}H_{14}O_{12}$	412.04	0.14%	0.01%	Molteni et al. (2018) Garmash et al. (2020)
	$C_{12}H_{14}O_{13}$	428.03	0.14%	0.02%	
	$C_{12}H_{14}O_{14}$	444.03	0.09%	/	Molteni et al. (2018) Garmash et al. (2020)
Nitrogen-containing product	$C_6H_5NO_3$	201.02	/	38.8%	Huang et al. (2014)
	$C_6H_5NO_4$	217.01	/	27.6%	Huang et al. (2014)
	$C_6H_4N_2O_6$	262.00	/	2.7%	Huang et al. (2014)
	$C_4H_5NO_5$	209.01	/	0.2%	
	$C_6H_7NO_5$	235.02	/	1.0%	
	$C_5H_5NO_6$	237.00	/	0.3%	
	$C_4H_5NO_7$	241.00	/	1.8%	
	$C_6H_5NO_6$	249.00	/	0.6%	
	$C_6H_7NO_6$	251.02	/	0.5%	
	$C_5H_5NO_7$	253.00	/	0.3%	
	$C_5H_7NO_7$	255.01	/	0.4%	
	$C_4H_5NO_8$	256.99	/	0.7%	
	$C_6H_7NO_7$	267.01	/	0.9%	
	$C_5H_5NO_8$	268.99	/	0.4%	
	$C_5H_7NO_8$	271.01	/	0.2%	
	$C_6H_5NO_8$	280.99	/	0.5%	
	$C_6H_7NO_8$	283.01	/	1.2%	
	$C_6H_9NO_8$	285.02	/	0.4%	
	$C_6H_7NO_9$	299.00	/	1.1%	
	$C_6H_9NO_9$	301.02	/	0.4%	
	$C_6H_8N_2O_9$	314.01	/	0.7%	
	$C_6H_7NO_{10}$	315.00	/	0.4%	

[*] RH = 24.3%, T = 24.4 °C, $OH_{exp} = 1.4 \times 10^{12}$ molecules cm^{-3}, HO_2 = 2.3 ppb.

[#] RH = 48.5%, T = 24.7 °C, $OH_{exp} = 3.7 \times 10^{11}$ molecules cm^{-3}, HO_2 = 0.6 ppb, NO = 3.2 ppb.

Table S3. The peak list and relative signal contributions (%) of major gaseous products produced by the toluene oxidation experiments shown in Fig. 1c-d.

Category	Formula	*m*/*z* (Th)	Percentage in total fitted signal		Listed by other studies of aromatic oxidation
			Exp. #16* (low NO_x)	Exp. #26# (high NO_x)	
Fragmented product	$C_2H_4O_4$	154.00	11.3%	0.2%	
	$C_3H_4O_5$	181.99	3.0%	0.2%	Mehra et al. (2020)
	$C_4H_2O_5$	191.98	0.7%	5.7%	
	$C_4H_4O_5$	193.99	7.2%	0.6%	Schwantes et al. (2017) Mehra et al. (2020)
	$C_4H_6O_5$	196.01	9.1%	0.1%	Mehra et al. (2020)
	$C_4H_4O_6$	209.99	1.1%	0.6%	Mehra et al. (2020)
	$C_5H_8O_5$	210.03	1.0%	0.1%	Mehra et al. (2020)
	$C_5H_4O_6$	221.99	8.6%	0.2%	Mehra et al. (2020)
Closed-shell monomeric product	$C_7H_8O_4$	218.03	0.3%	0.3%	Schwantes et al. (2017) Molteni et al. (2018) Zaytsev et al. (2019)
	$C_7H_6O_5$	232.01	0.3%	0.3%	Zaytsev et al. (2019) Mehra et al. (2020)
	$C_7H_8O_5$	234.03	1.5%	0.4%	Schwantes et al. (2017) Molteni et al. (2018) Zaytsev et al. (2019) Mehra et al. (2020)
	$C_6H_6O_6$	236.01	5.0%	0.2%	Molteni et al. (2018) Mehra et al. (2020)
	$C_7H_{10}O_5$	236.04	0.8%	0.2%	Molteni et al. (2018) Zaytsev et al. (2019) Garmash et al. (2020) Mehra et al. (2020)
	$C_6H_8O_6$	238.02	2.0%	0.4%	Molteni et al. (2018) Mehra et al. (2020)
	$C_7H_6O_6$	248.01	0.8%	/	Zaytsev et al. (2019)
	$C_7H_8O_6$	250.02	5.3%	0.6%	Molteni et al. (2018) Zaytsev et al. (2019) Mehra et al. (2020)
	$C_6H_6O_7$	252.00	0.9%	0.4%	Molteni et al. (2018) Mehra et al. (2020)
	$C_7H_{10}O_6$	252.04	2.9%	0.8%	Molteni et al. (2018) Zaytsev et al. (2019) Mehra et al. (2020)
	$C_6H_8O_7$	254.02	1.6%	0.7%	Molteni et al. (2018) Garmash et al. (2020)
	$C_7H_{12}O_6$	254.05	0.1%	0.1%	Molteni et al. (2018) Mehra et al. (2020)
	$C_6H_{10}O_7$	256.03	0.4%	0.1%	
	$C_7H_6O_7$	264.00	1.0%	/	
	$C_7H_8O_7$	266.02	3.6%	0.4%	Mehra et al. (2020)
	$C_6H_6O_8$	268.00	0.2%	0.1%	
	$C_7H_{10}O_7$	268.03	4.3%	0.2%	Molteni et al. (2018) Mehra et al. (2020)
	$C_6H_8O_8$	270.01	0.6%	/	Molteni et al. (2018) Garmash et al. (2020)
	$C_7H_{12}O_7$	270.05	1.0%	0.1%	Molteni et al. (2018)
	$C_7H_6O_8$	280.00	0.5%	0.2%	
	$C_7H_8O_8$	282.01	2.3%	0.4%	Molteni et al. (2018)
	$C_7H_{10}O_8$	284.03	2.9%	0.8%	Molteni et al. (2018)
	$C_7H_{12}O_8$	286.04	1.5%	0.2%	Molteni et al. (2018)
	$C_7H_8O_9$	298.01	0.3%	0.5%	
	$C_7H_{10}O_9$	300.02	1.9%	0.8%	Molteni et al. (2018)
	$C_7H_{12}O_9$	302.04	0.6%	/	
	$C_7H_8O_{10}$	314.00	0.4%	/	
	$C_7H_{10}O_{10}$	316.02	0.6%	1.1%	Molteni et al. (2018)

	$C_7H_{12}O_{10}$	318.03	0.3%	/	
Open-shell monomeric product	$C_7H_9O_5$	235.03	0.1%	0.2%	
	$C_7H_7O_6$	249.01	0.3%	0.01%	
	$C_7H_7O_7$	265.01	0.2%	/	
	$C_7H_9O_7$	267.02	0.7%	2.3%	
	$C_7H_9O_9$	299.01	1.5%	1.2%	Molteni et al. (2018)
	$C_7H_9O_{10}$	315.01	0.6%	0.1%	
Dimeric product	$C_{14}H_{18}O_8$	376.09	0.06%	/	Molteni et al. (2018) Garmash et al. (2020)
	$C_{14}H_{18}O_{10}$	408.08	0.15%	0.02%	Molteni et al. (2018)
	$C_{14}H_{16}O_{11}$	422.06	0.11%	0.07%	
	$C_{14}H_{18}O_{11}$	424.07	0.12%	0.02%	Molteni et al. (2018)
	$C_{14}H_{20}O_{11}$	426.09	0.15%	0.00%	Molteni et al. (2018)
	$C_{14}H_{16}O_{12}$	438.05	0.11%	0.14%	
	$C_{14}H_{18}O_{12}$	440.07	0.18%	0.07%	Molteni et al. (2018)
	$C_{14}H_{20}O_{12}$	442.08	0.08%	/	
	$C_{14}H_{18}O_{14}$	472.06	0.11%	/	Molteni et al. (2018)
Nitrogen-containing product	$C_6H_5NO_3$	201.02	/	15.6%	Huang et al. (2014)
	$C_7H_7NO_3$	215.03	/	8.7%	
	$C_6H_5NO_4$	217.01	/	4.4%	Huang et al. (2014)
	$C_7H_7NO_4$	231.03	/	2.4%	
	$C_6H_4N_2O_6$	262.00	/	0.3%	Huang et al. (2014)
	$C_4H_5NO_5$	209.01	/	0.2%	
	$C_7H_5NO_4$	229.01	/	1.1%	Zaytsev et al. (2019)
	$C_5H_5NO_6$	237.00	/	0.4%	
	$C_7H_9NO_5$	249.04	/	1.0%	Zaytsev et al. (2019)
	$C_5H_5NO_7$	253.00	/	0.7%	
	$C_6H_9NO_6$	253.03	/	0.7%	
	$C_5H_7NO_7$	255.01	/	2.1%	
	$C_7H_7NO_6$	263.02	/	0.9%	Zaytsev et al. (2019)
	$C_7H_9NO_6$	265.03	/	2.0%	Zaytsev et al. (2019)
	$C_6H_8N_2O_6$	266.03	/	0.6%	
	$C_6H_7NO_7$	267.01	/	0.6%	
	$C_6H_9NO_7$	269.03	/	1.1%	Tsiligiannis et al. (2019)
	$C_5H_7NO_8$	271.01	/	1.4%	
	$C_7H_9NO_7$	281.03	/	3.4%	Zaytsev et al. (2019)
	$C_6H_9NO_8$	285.02	/	1.4%	
	$C_7H_7NO_8$	295.01	/	0.7%	
	$C_7H_9NO_8$	297.02	/	5.8%	Zaytsev et al. (2019)
	$C_7H_7NO_9$	311.00	/	0.6%	
	$C_7H_9NO_9$	313.02	/	2.8%	
	$C_6H_8N_2O_9$	314.01	/	0.5%	
	$C_7H_{11}NO_9$	315.03	/	2.0%	
	$C_7H_{10}N_2O_9$	328.03	/	1.0%	
	$C_7H_9NO_{10}$	329.01	/	1.7%	

[*] RH = 28.3%, T = 24.3°C, $OH_{exp} = 1.5 \times 10^{12}$ molecules cm^{-3}, HO_2 = 2.3 ppb.

[#] RH = 52.9%, T = 23.2 °C, $OH_{exp} = 3.7 \times 10^{11}$ molecules cm^{-3}, HO_2 = 0.6 ppb, NO = 3.0 ppb.

Table S4. Experimental conditions and gaseous oxygenated products for the photooxidation of benzene in previous studies and this study. We normalize the abundance of all listed ions to that of $C_6H_7O_9$ which is a commonly observed RO_2 radical for comparison.

Conditions and Products	Molteni et al. (2018) Flow tube	Garmash et al. (2020) Flow tube	Garmash et al. (2020) JPAC	This study OFR (Exp. #2)
Experimental conditions				
Residence time	20 s	10 s	48 min	95 s
[Benzene] (molecules cm^{-3})	9.85×10^{13}	$\sim 1.00 \times 10^{16}$	7.22×10^{10}	2.72×10^{12}
[OH] (molecules cm^{-3})	$8.50 \times 10^{11*}$	N/A	4.46×10^{8}	1.67×10^{10}
[Benzene]:[OH]	116	N/A	162	163
Relative proportion of oxygenated products (normalize to the signal of $C_6H_7O_9$)				
$C_6H_7O_5$	/	0.02	/	0.14
$C_6H_7O_7$	/	0.05	/	0.57
$C_6H_7O_9$	1	1	1	1
$C_6H_8O_5$	12.82	1.09	/	0.57
$C_6H_8O_7$	1.55	0.35	3.99	3.43
$C_6H_8O_9$	2.36	1.70	3.48	1.57
$C_{12}H_{14}O_8$	5.55	1.73	0.29	0.09
$C_{12}H_{14}O_{10}$	0.64	0.48	0.55	0.19
$C_{12}H_{14}O_{12}$	1.18	1.27	0.57	0.20
$C_{12}H_{14}O_{14}$	1.64	0.32	0.38	0.13

* The OH concentration in this study refers to the initial OH concentration.

Table S5. Potential product formulae (oxygen number $\geqslant$ 5) from a second OH attack in benzene and toluene oxidation (y means hydrogen numbers of products).

	H_y- series products		H_{y+2}- series products	
Second OH attack	H abstraction	OH addition	H abstraction	OH addition
	Hydrogen number		Hydrogen number	
Radical	y-1	y+1	y+1	y+3
Carbonyl	y-2	y	y	y+2
Alcohol	y	y+2	y+2	y+4
Hydroperoxide	y	y+2	y+2	y+4